

Tuning moiré excitons and correlated electronic states through layer degree of freedom

Received: 14 November 2021

Accepted: 29 July 2022

Published online: 16 August 2022

 Check for updates

Dongxue Chen^{1,2,10}, Zhen Lian^{2,10}, Xiong Huang^{3,4,10}, Ying Su^{5,10}, Mina Rashetnia³, Li Yan², Mark Blei⁶, Takashi Taniguchi⁷, Kenji Watanabe⁸, Sefaattin Tongay⁶, Zenghui Wang¹✉, Chuanwei Zhang⁵✉, Yong-Tao Cui³✉ & Su-Fei Shi^{2,9}✉

Moiré coupling in transition metal dichalcogenides (TMDCs) superlattices introduces flat minibands that enable strong electronic correlation and fascinating correlated states, and it also modifies the strong Coulomb-interaction-driven excitons and gives rise to moiré excitons. Here, we introduce the layer degree of freedom to the WSe₂/WS₂ moiré superlattice by changing WSe₂ from monolayer to bilayer and trilayer. We observe systematic changes of optical spectra of the moiré excitons, which directly confirm the highly interfacial nature of moiré coupling at the WSe₂/WS₂ interface. In addition, the energy resonances of moiré excitons are strongly modified, with their separation significantly increased in multilayer WSe₂/monolayer WS₂ moiré superlattice. The additional WSe₂ layers also modulate the strong electronic correlation strength, evidenced by the reduced Mott transition temperature with added WSe₂ layer(s). The layer dependence of both moiré excitons and correlated electronic states can be well described by our theoretical model. Our study presents a new method to tune the strong electronic correlation and moiré exciton bands in the TMDCs moiré superlattices, ushering in an exciting platform to engineer quantum phenomena stemming from strong correlation and Coulomb interaction.

In a strongly correlated electronic system, Coulomb interactions among electrons dominate over kinetic energy. Recently, two-dimensional (2D) moiré superlattices of van der Waals materials have emerged as a promising platform to study correlated physics and exotic quantum phases in 2D, such as the correlated insulating states

and superconductivity in graphene moiré superlattices^{1–14}, the Mott insulator state at half band filling and various generalized Wigner crystal states at fractional fillings of the moiré superlattices based on transition metal dichalcogenides (TMDCs)^{15–23}. The key to the strong correlation in these systems is the enhanced Coulomb interaction in

¹Institute of Fundamental and Frontier Sciences, University of Electronic Science and Technology of China, Chengdu, Sichuan, China. ²Department of Chemical and Biological Engineering, Rensselaer Polytechnic Institute, Troy, NY 12180, USA. ³Department of Physics and Astronomy, University of California, Riverside, CA 92521, USA. ⁴Department of Materials Science and Engineering, University of California, Riverside, CA 92521, USA. ⁵Department of Physics, University of Texas at Dallas, Dallas, TX 75083, USA. ⁶School for Engineering of Matter, Transport and Energy, Arizona State University, Tempe, AZ 85287, USA. ⁷International Center for Materials Nanoarchitectonics, National Institute for Materials Science, 1-1 Namiki, Tsukuba 305-0044, Japan. ⁸Research Center for Functional Materials, National Institute for Materials Science, 1-1 Namiki, Tsukuba 305-0044, Japan. ⁹Department of Electrical, Computer & Systems Engineering, Rensselaer Polytechnic Institute, Troy, NY 12180, USA. ¹⁰These authors contributed equally: Dongxue Chen, Zhen Lian, Xiong Huang, Ying Su. ✉e-mail: zenghui.wang@uestc.edu.cn; Chuanwei.Zhang@utdallas.edu; yongtao.cui@ucr.edu; shis2@rpi.edu

2D and greatly reduced kinetic energy in the flat moiré minibands. In TMDC-based moiré superlattices, the combination of large effective mass and strong moiré coupling renders the easier formation of flat bands and stronger electronic correlation, compared with graphene moiré superlattices. For example, the 0- or 60-degree angle-aligned WSe_2/WS_2 exhibits Mott insulating states with transition temperatures exceeding 150 K^{18,19}, the highest among all 2D moiré systems studied so far. It also hosts various correlated insulating states at fractional fillings of the moiré lattice^{18,19}, indicating strong and long-range electron interactions.

Meanwhile, the strong Coulomb interaction in 2D also leads to tightly bound excitons with large binding energy in TMDCs^{24–27}. The moiré coupling in the TMDC moiré superlattices is expected to generate excitonic flat minibands²⁸, beyond the single-particle electronic flat bands in the conduction and valence bands. Recently, the moiré excitons have been reported in the angle-aligned WSe_2/WS_2 heterojunction^{17,18}, in which correlated insulating states also occur^{15,17–19}. The excitonic flat band is promising for realizing topological exciton states and correlated exciton Hubbard model^{28,29}, ushering in exciting opportunities for engineering correlated quantum states. However, there are key questions that remained to be addressed. For example, how is the moiré coupling's extension in the out-of-plane direction? How could one systematically tune both the electronic flat bands and moiré exciton bands in the TMDCs moiré superlattice?

In this work, we investigate these questions utilizing the layer degree of freedom, inspired by the layer-layer coupling in TMDCs that leads to the abrupt direct-to-indirect bandgap transition from monolayer to bilayer TMDCs^{30,31}. We demonstrate a general approach tuning both electronic and moiré exciton bands by increasing the layer

number of WSe_2 in the angle-aligned WSe_2/WS_2 heterojunction. As the layer number of WSe_2 varies from monolayer (1L) to bilayer (2L) and trilayer (3L), the optical spectra of the moiré exciton change systematically in a way that suggests the moiré coupling is highly interfacial, strongly confined at the WSe_2/WS_2 interface and barely affects the next neighboring WSe_2 layer(s). However, the added WSe_2 layer(s) could modify moiré excitons in the WSe_2 layer interfacing WS_2 , resulting in a significant increase in the resonance energy separations between moiré excitons. This observation can be well described by a phenomenological model. Our work, to our best knowledge, reports the first sensitive tuning of moiré excitons via layer degree of freedom.

The correlated electronic structure is also sensitive to the number of layers in WSe_2 . The Mott insulator state at the filling of one hole per moiré unit cell ($n = -1$) is found to have a transition temperature decreased from 180 K in 1L/1L WSe_2/WS_2 to 120 K in 2L/1L WSe_2/WS_2 and 60 K in 3L/1L WSe_2/WS_2 . The correlated states at fractional fillings (fractional charge per moiré supercell) are significantly quenched in the 3L/1L WSe_2/WS_2 heterojunction. The reduced Mott transition temperature, however, is still significantly higher than that of graphene moiré superlattices (~ 4 K). Our study, therefore, also demonstrates a new knob to tune the strong electron correlation in TMDC moiré superlattices that can be further exploited for engineering new correlated quantum states.

Results and discussion

The back-gated angle-aligned WSe_2/WS_2 heterojunction device is schematically shown in Fig. 1a, which includes three different regions in the same device: 1L/1L WSe_2/WS_2 , 2L/1L WSe_2/WS_2 , and 3L/1L WSe_2/WS_2 . The device was constructed through a dry pickup method described previously¹³ (also see Methods), and the heterojunctions are

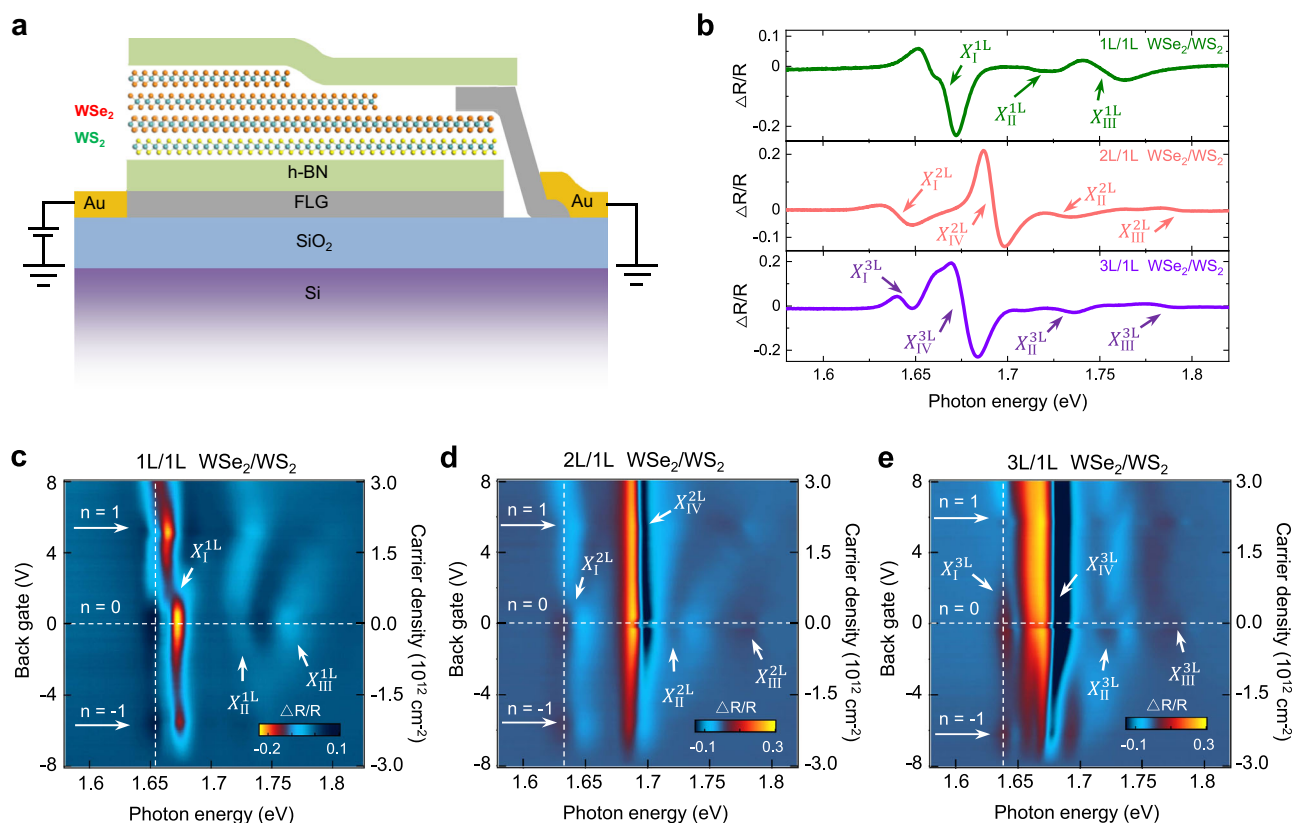


Fig. 1 | Angle-aligned multilayer WSe_2 /monolayer WS_2 moiré superlattice.

a Schematic of the multilayer WSe_2 /monolayer WS_2 heterojunction devices, with the heterojunctions encapsulated with flakes of BN on both sides. The few-layer-graphene (FLG) works as the back gate electrode. **b** Differential reflectance spectra

of different regions at zero gate voltage. **c–e** are the differential reflectance spectra as a function of the gate voltage (density of carriers) at the region of 1L/1L, 2L/1L, and 3L/1L WSe_2/WS_2 . All data were taken at 4.5 K.

encapsulated with flakes of boron nitride (BN) and gated through few-layer graphene flake working as the back gate electrode. WSe₂ and WS₂ have a lattice mismatch of ~4%, resulting in a moiré superlattice with a periodicity of ~8 nm^{32,33} when they are angle-aligned (0- or 60-degree twisted). Having the three regions (1L/1L WSe₂/WS₂, 2L/1L WSe₂/WS₂, and 3L/1L WSe₂/WS₂) in the same device is advantageous as these three regions have the same twist angle since the WSe₂ for all these three regions are from the same flake. As a result, the moiré lattice constant in these three regions are about the same, and we can compare our measurements from these different regions directly.

The 1L/1L WSe₂/WS₂ heterojunction has a type-II band alignment, with the conduction band minimum located in the WS₂ layer and the valence band maximum in the WSe₂ layer¹⁵. Strong moiré coupling leads to a band folding in the mini-Brillouin zone and generates moiré exciton bands³², which will split the A exciton resonance of WSe₂ into three moiré exciton peaks, as demonstrated in the previous experiments^{17,32}. Here we measure the reflectance spectra in the three different regions of the WSe₂/WS₂ heterojunction as a function of the gate voltage, with results shown in Fig. 1c–e. There are two major differences between the moiré exciton spectra from the 1L/1L WSe₂/WS₂ and multilayer WSe₂/monolayer WS₂ (2L/1L WSe₂/WS₂ or 3L/1L WSe₂/WS₂) heterojunctions. First, it is evident that near the charge-neutral region (gate voltage 0 V), there are three moiré exciton resonances in the 1L/1L WSe₂/WS₂ region (Fig. 1c) but four in both 2L/1L (Fig. 1d) and 3L/1L (Fig. 1e) WSe₂/WS₂ regions. Second, the moiré exciton energy difference between the lowest and highest energy moiré excitons increases significantly in both 2L/1L (Fig. 1d) and 3L/1L (Fig. 1e) WSe₂/WS₂ regions. These observations are better illustrated in Fig. 1b, which plots the differential reflectance spectra at the gate voltage of 0 V for the three different regions (line cuts at zero gate voltage in Fig. 1c–e). For the 1L/1L WSe₂/WS₂ region, we observe three moiré exciton peaks at -1.662 eV (X_1^{1L}), 1.715 eV (X_{II}^{1L}), and 1.753 eV (X_{III}^{1L}), consistent with the previous reports³². However, in the 2L/1L WSe₂/WS₂ region, one additional exciton resonance emerges, adding up to a total of four major excitons peaked at -1.642 eV (X_1^{2L}), -1.693 eV (X_{IV}^{2L}), 1.728 eV (X_{II}^{2L}), and 1.793 eV (X_{III}^{2L}). In the 3L/1L WSe₂/WS₂ region, there are also four major exciton resonances at -1.645 eV (X_1^{3L}), -1.677 eV (X_{IV}^{3L}), 1.730 eV (X_{II}^{3L}), and 1.785 eV (X_{III}^{3L}). The largest moiré exciton energy difference, defined as the energy difference between X_{III} and X_I , is -90 meV for the 1L/1L WSe₂/WS₂ region but -150 meV for 1L/2L WSe₂/WS₂ region and -140 meV for 1L/3L WSe₂/WS₂ region, an increase of more than 50%. Similar behaviors have been observed for all the devices we have studied (details in Supplementary Note 5).

Our observations suggest that the moiré potential is highly localized at the WSe₂/WS₂ interface and has a limited extension along the out-of-plane direction. As a result, the moiré coupling only significantly modifies the first WSe₂ layer in contact with the monolayer WS₂. The newly developed exciton resonances in the 2L/1L and 3L/1L WSe₂/WS₂ heterojunctions (X_{IV}^{2L} and X_{IV}^{3L}), therefore, arise from the barely modified intralayer A exciton in the upper WSe₂ layers away from the interface (also see Supplementary Note 1). Our interpretation is supported by the fact that the energies of X_{IV}^{2L} (1.693 eV) and X_{IV}^{3L} (1.677 eV) are close to the intralayer A exciton energy of monolayer WSe₂ (-1.70 eV), and it is further corroborated by the stronger reflectance intensity from the new moiré exciton in 3L/1L WSe₂/WS₂ (X_{IV}^{3L}) compared with that in 2L/1L WSe₂/WS₂ (X_{IV}^{2L}). Moreover, there is a redshift in the moiré exciton resonance X_I and blueshifts in X_{II} and X_{III} in both 2L/1L and 3L/1L WSe₂/WS₂ compared with those in 1L/1L WSe₂/WS₂ (Fig. 1b). And the shift of X_{II} and X_{III} is more significant in magnitude than that of X_I .

Our results can be understood with a phenomenological model (details in Supplementary Note 2), considering the moiré excitons in the first WSe₂ layer interacting with an exciton state in the added WSe₂ layer (s) that has the resonance energy between X_I and X_{II} . The resulting level repulsion naturally explains the redshift of X_I and blue shift of X_{II} and X_{III} in the 2L/1L (3L/1L) WSe₂/WS₂ compared with 1L/1L WSe₂/WS₂. To

understand the phenomenological model, we propose a possible microscopic mechanism by considering the hybridization between moiré excitons and interlayer-like hybrid exciton (iX) in multilayer WSe₂/1L WS₂ (details in Supplementary Information Note 2). The hybridization can increase the energy separation between moiré excitons and is enabled by the moiré-potential-induced Umklapp scattering^{34–36}. The interlayer-like hybrid exciton arises from the interlayer tunneling in multilayer WSe₂ that hybridizes the valence bands in different layers³⁷. However, it has much weaker oscillator strength than the intralayer-like hybrid exciton and cannot be resolved in the experiment. In the absence of hybridization between different excitonic states, the energy dispersion of bare intralayer A excitons in 1L WSe₂ and moiré excitons in 1L/1L WSe₂/WS₂ are shown in Fig. 2a, b, respectively. Here we fold the energy bands of A excitons into the mini-Brillouin zone to compare directly with that of moiré excitons. The bright A exciton state at the mini-Brillouin zone center (which is denoted as γ point as shown in the inset of Fig. 2a) is marked as X_A in Fig. 2a, and the bright moiré exciton states are marked as X_I^{1L} , X_{II}^{1L} , and X_{III}^{1L} in Fig. 2b. The optical absorption spectrum of moiré excitons in 1L/1L WSe₂/WS₂ is shown in Fig. 2c, with the three resonances corresponding to the three bright moiré exciton states. For the absorption spectrum of 2L/1L WSe₂/WS₂ in Fig. 2d, we introduce the hybridization between moiré excitons and interlayer-like hybrid excitons (see Supplementary Information Note 2). The hybridization induces a redshift in X_I^{2L} and blueshifts in X_{II}^{2L} and X_{III}^{2L} compared with those of 1L/1L WSe₂/WS₂ in Fig. 2c. The larger shift in the magnitude of X_{II}^{2L} and X_{III}^{2L} indicates stronger hybridization with the interlayer-like hybrid exciton, which is consistent with the proposed mechanism (see Supplementary Information Note 2).

Moreover, the intralayer-like hybrid exciton in the second WSe₂ layer leads to another resonance X_{IV}^{2L} between X_I^{2L} and X_{II}^{2L} , as shown in Fig. 2d, which is consistent with our experimental observation (Fig. 1b, d). In 3L/1L WSe₂/WS₂, additional hybrid excitons can be induced by the interlayer tunneling between valence bands in the 2nd and 3rd WSe₂ layers. In this case, the additional hybrid excitons away from the WSe₂/WS₂ interface do not affect the moiré excitons. Therefore, the moiré excitons in 3L/1L WSe₂/WS₂ are nearly identical to those in 2L/1L WSe₂/WS₂ (Fig. 2d), also consistent with our experimental results (Fig. 1b). On the other hand, the additional hybrid excitons from upper WSe₂ layers will contribute to the resonant peak X_{IV}^{3L} which should be consisted of two sub-resonances. This is also consistent with our experimental data, as X_{IV}^{3L} (Fig. 1e) is broader than X_{IV}^{2L} (Fig. 1d). Interestingly, although these two resonances in X_{IV}^{3L} cannot be resolved at the charge-neutral region, likely due to linewidth broadening, they can be revealed in the p-doping region (Fig. 1e). The exact mechanism will be investigated in the future.

The moiré excitons in the three regions show distinct gate dependence, which also confirms the interfacial nature of the moiré coupling in the WSe₂/WS₂ superlattice. Our theoretical model, which considers the interfacial nature of the moiré coupling, shows that the valence bands due to the added layers are higher in energy than the moiré electronic flat band from the WSe₂/WS₂ interface, as shown in Fig. 3a–c (detailed calculations in Supplementary Information Note 3). When carriers are added to the 1L/1L WSe₂/WS₂ heterostructure, they will fill the first moiré valence band in the WSe₂ layer and the first moiré conduction band in the WS₂ layer. The first flat moiré miniband has a strong electron correlation due to their narrow bandwidth, and at the half-filling states (one electron/hole per moiré unit cell, $n = +1$ or -1), Mott insulator states will occur, as demonstrated in several recent experiments^{15–20}. The optical reflectance spectra are expected to be modulated by these correlated states. In the 1L/1L WSe₂/WS₂ region, all three excitons are modulated, with X_I^{1L} being the most obvious one (Fig. 1c). In the 2L/1L and 3L/1L WSe₂/WS₂ regions, the excitons at the lowest energy (X_I^{2L} and X_I^{3L}) are also strongly modulated (Fig. 1d, e). Figure 3d–f plots the gate voltage dependence of the lowest energy

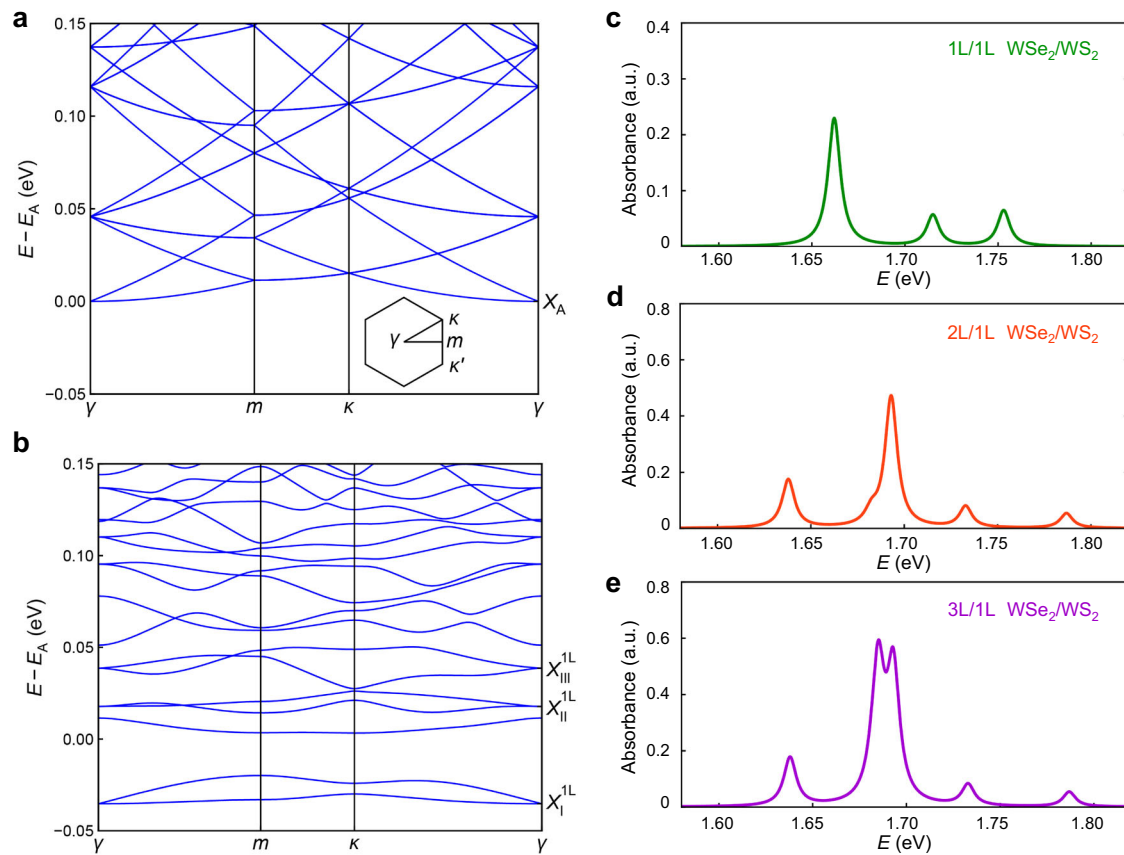


Fig. 2 | Theoretical simulation of moiré excitons. **a, b** are the energy bands of bare intralayer A excitons in 1L WSe₂ and moiré excitons in 1L/1L WSe₂/WS₂, respectively. **a** The A exciton bands are folded into the mini-Brillouin zone of the moiré superlattice to compare directly with that of moiré excitons in **b**. Inset of **a** shows the schematic of the mini-Brillouin zone and the label of high symmetry points. The WSe₂ bright intralayer A exciton state is marked by X_A in **a**. The three

bright Moiré exciton states are marked by X_I^{1L} , X_{II}^{1L} , and X_{III}^{1L} in **b**. Here, we set the energy E_A of X_A as the energy reference. **c–e** Optical absorption spectra in 1L/1L, 2L/1L, and 3L/1L WSe₂/WS₂. The interlayer hybridization between moiré exciton and intralayer A exciton is considered in **d** and **e**, with details elaborated in Supplementary Information Note 2.

moiré exciton for the three different regions (X_I^{1L} , X_{II}^{1L} and X_{III}^{1L}), which clearly shows intensity modulations at $n = -1$ and $+1$. On the other hand, the additional excitons in 2L/1L (X_{IV}^{2L}) and 3L/1L (X_{IV}^{3L}) WSe₂/WS₂ regions are barely affected by the formation of the Mott states at $n = \pm 1$ (Fig. 1d, e). These behaviors can also be explained by the interfacial nature of the moiré coupling, which confines the correlated electrons at the interface of WSe₂/WS₂. The modulation of the moiré excitons at the $n = \pm 1$ is likely due to the dielectric constant change and gap opening associated with the Mott insulator states. Due to the small radius of the strongly bound exciton²⁴, only the moiré excitons in the first WSe₂ layer immediately interfacing with the WS₂ monolayer can sensitively detect the dielectric constant change at the interface. In the 2L/1L and 3L/1L regions, the additional excitons originated from intralayer excitons localized in the added layers, are thus barely affected.

To better investigate the tuning of the electron correlation by the layer degree of freedom, we perform microwave impedance microscopy (MIM) measurements to study the correlated insulating states in the three different heterostructure regions (Fig. 4a). MIM probes the local conductivity of the sample and has been successfully employed to reveal a rich structure of correlated insulating states in the angle-aligned 1L/1L WSe₂/WS₂ device⁸. In the multilayer WSe₂/1L WS₂ device, we primarily focus on the features on the hole side, as the holes reside in the WSe₂ layer due to the type-II alignment, and we introduce the layer degree of freedom by modulating the layer number of WSe₂. At temperature $T = 10$ K, the MIM spectra in both 1L/1L and 2L/1L WSe₂/WS₂ regions show similar pronounced features at various fillings, including

the Mott insulator states at $n = -1$, the generalized Wigner crystal states at fractional fillings of $n = -1/3$ & $-2/3$, $-1/2$, $-1/4$ & $-3/4$, etc. The 3L/1L WSe₂/WS₂ data show fewer and less pronounced dips: other than the Mott insulator state at $n = -1$, only two fractional fillings $n = -1/3$ and $-1/2$ can be resolved. There is also a small difference in the twist angle in the 3L/1L WSe₂/WS₂ region (-1.3°) compared to that in the 1L/1L and 2L/1L regions (-0.9°), which results in different gate voltage positions for these insulating states in the 3L/1L WSe₂/WS₂ region (details in method). Since the formation of the correlated insulating states at fractional fillings depends on long-range Coulomb interaction among electrons in neighboring moiré unit cells, our results suggest that the inter-site electron interaction strength is weaker in 3L/1L than in 1L/1L or 2L/1L WSe₂/WS₂. The difference in the on-site interaction, corresponding to the Mott insulator state at $n = -1$, can be further revealed in its temperature dependence. As shown in Fig. 4b–d, as the temperature is raised, the features at fractional fillings disappear at -30 K in both 1L/1L and 2L/1L WSe₂/WS₂ regions and at -15 K in the 3L/1L WSe₂/WS₂ region. The Mott insulator state at $n = -1$ survives at much higher temperatures in 1L/1L WSe₂/WS₂, persisting to above 180 K, the highest Mott transition temperature reported in all 2D moiré superlattice structures so far. In the 2L/1L WSe₂/WS₂ region, the Mott transition temperature is -120 K, while it is much lower, -60 K, in the 3L/1L region. As the correlation strength is determined by the ratio of the Coulomb interaction to the kinetic energy, the reduction of electron correlation strength from 1L/1L or 2L/1L WSe₂/WS₂ is likely due to the increased dielectric screening from the added WSe₂, which reduces the Coulomb

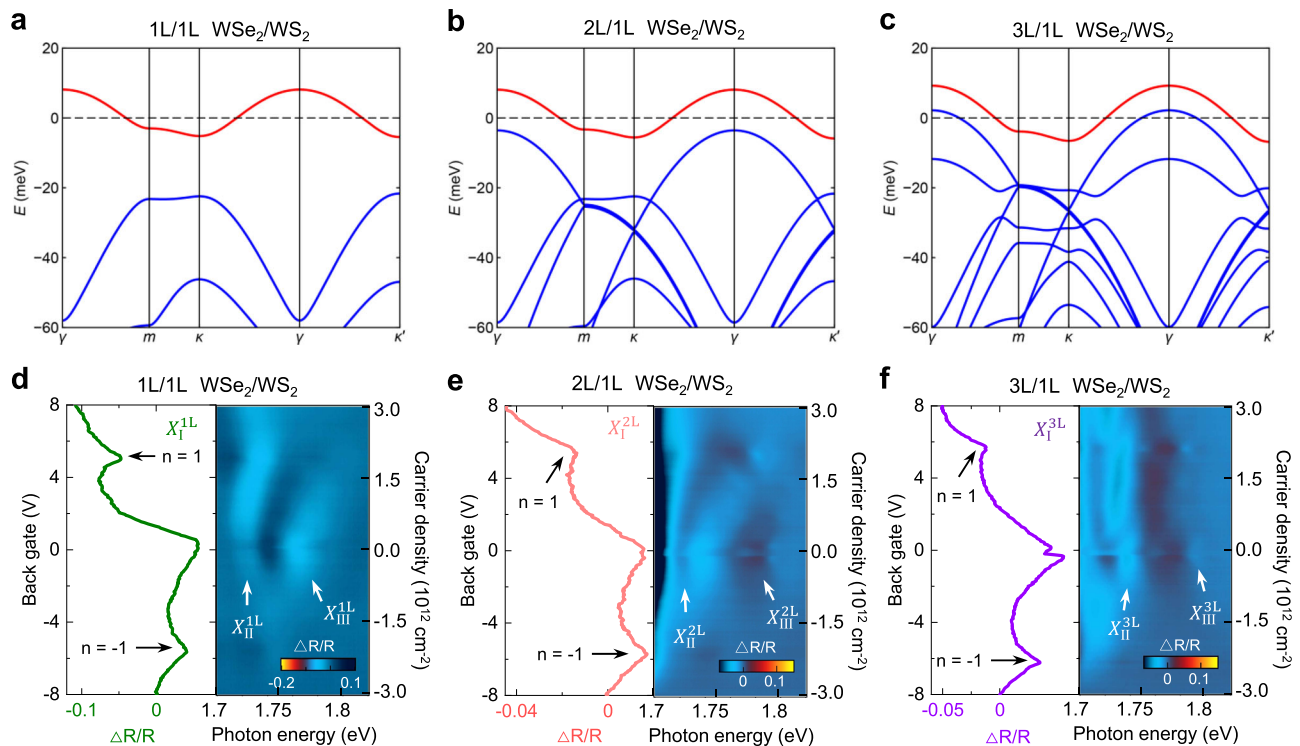


Fig. 3 | Layer dependence of the electronic flat miniband for WSe₂/WS₂ moiré superlattices. **a–c** are calculated electronic bandstructure of the valence band in 1L/1L WSe₂/WS₂, 2L/1L WSe₂/WS₂, 3L/1L WSe₂/WS₂, respectively (details in Supplementary Information Note 3), with the moiré flat band from the 1st layer WSe₂

labeled in red. **d–f** are differential reflectance intensity of the lowest energy moiré exciton (X_I) as a function of the back gate voltage (carrier density) in Fig. 1c–e, respectively (vertical dashed line cuts), with the 2D color plots showing the enhanced reflectance spectra near the moiré excitons X_{II} and X_{III} .

interaction at the interface. However, the further reduced correlation strength in the 3L/1L WSe₂/WS₂ is facilitated by the additional increase of kinetic energy, which arises from the increased bandwidth of the flat band, according to our calculation shown in Supplementary Information Fig. 2. We emphasize here that even the reduced electron correlation in the 2L/1L and 3L/1L WSe₂/WS₂ is still significantly stronger than that in graphene moiré systems, which has a Mott transition temperature ~ 4 K¹. As a result, the layer degree of freedom can be utilized for engineering new correlated states.

In summary, we have demonstrated a new moiré superlattice system based on multilayer TMDC heterojunctions. The added layers host additional intralayer excitons that interact with the moiré excitons residing at the moiré interface, and they can further modify the correlation strength of the correlated states. Considering the layer-valley-spin locking in TMDC³⁸, these new TMDCs moiré superlattices provide an exciting platform to investigate emerging correlated valley and spin physics.

Methods

Heterostructure device fabrication

We use a dry pickup method^{20,39} to fabricate the WSe₂/WS₂ heterostructures. We exfoliate monolayer WS₂, multilayer WSe₂, graphite, and BN layers on silicon substrate with a 285 nm thermal oxide layer. For angle-aligned heterostructures, we choose exfoliated WS₂ and WSe₂ layers with sharp edges, whose crystal axes are further confirmed by second harmonic generation measurements. We then mount the SiO₂/Si substrate on a rotational stage and clamp the glass slide with thin flakes to another three-dimensional (3D) stage. We adjust the 3D stage to control the distance between substrates and thin flakes, and we sequentially pickup different layers onto the pre-patterned Au electrodes on SiO₂/Si substrates. We fine adjust the angle of the rotational stage (accuracy of 0.02°) under a microscope objective to stack the WSe₂/WS₂ heterojunction, ensuring a near-zero twist angle

between the two flakes. The final constructed device is annealed at 130 °C for 12 hours in a vacuum chamber. The pre-patterned Au contact electrodes are fabricated through standard electron-beam lithography and e-beam evaporation processes (see Supplementary Information Fig. 3 for the optical microscope image of the device used in the main text). More sample characterization details can be found in Supplementary Note 4.

Optical spectroscopy measurements

To perform differential reflectance contrast measurement, the samples were mounted in a helium flow-controlled cryostat with a quartz optical window and electrical feedthroughs. A super-continuum laser (YSL Photonics) was used as the white light source. The laser was focused onto the sample with a $\times 50$ objective (the typical laser spot size is ~ 2 μ m). The reflected light was directed into a spectrograph and collected with a CCD camera (Princeton Instruments). The differential reflectance is calculated as $\frac{\Delta R}{R} = \frac{R - R_0}{R_0}$ by using the reflectance spectrum at the highest p-doping region as the reference R_0 .

Microwave impedance microscopy measurements

The MIM measurement is performed on a homebuilt cryogenic scanning probe microscope platform. A small microwave excitation of about 0.1 μ W at a fixed frequency ~ 10 GHz is delivered to a chemically etched tungsten tip mounted on a quartz tuning fork. The reflected signal is analyzed to extract the demodulated output channels, MIM-Im and MIM-Re, which are proportional to the imaginary and real parts of the admittance between the tip and sample, respectively. To enhance the MIM signal quality, the tip on the tuning fork is excited to oscillate at a frequency of around 32 kHz with an amplitude of ~ 8 nm. The resulting oscillation amplitudes of MIM-Im and MIM-Re are then extracted using a lock-in amplifier to yield $d(\text{MIM-Im})/dz$ and $d(\text{MIM-Re})/dz$, respectively. The $d(\text{MIM})/dz$ signals are free of fluctuating backgrounds, and their behavior is very similar to that of the standard

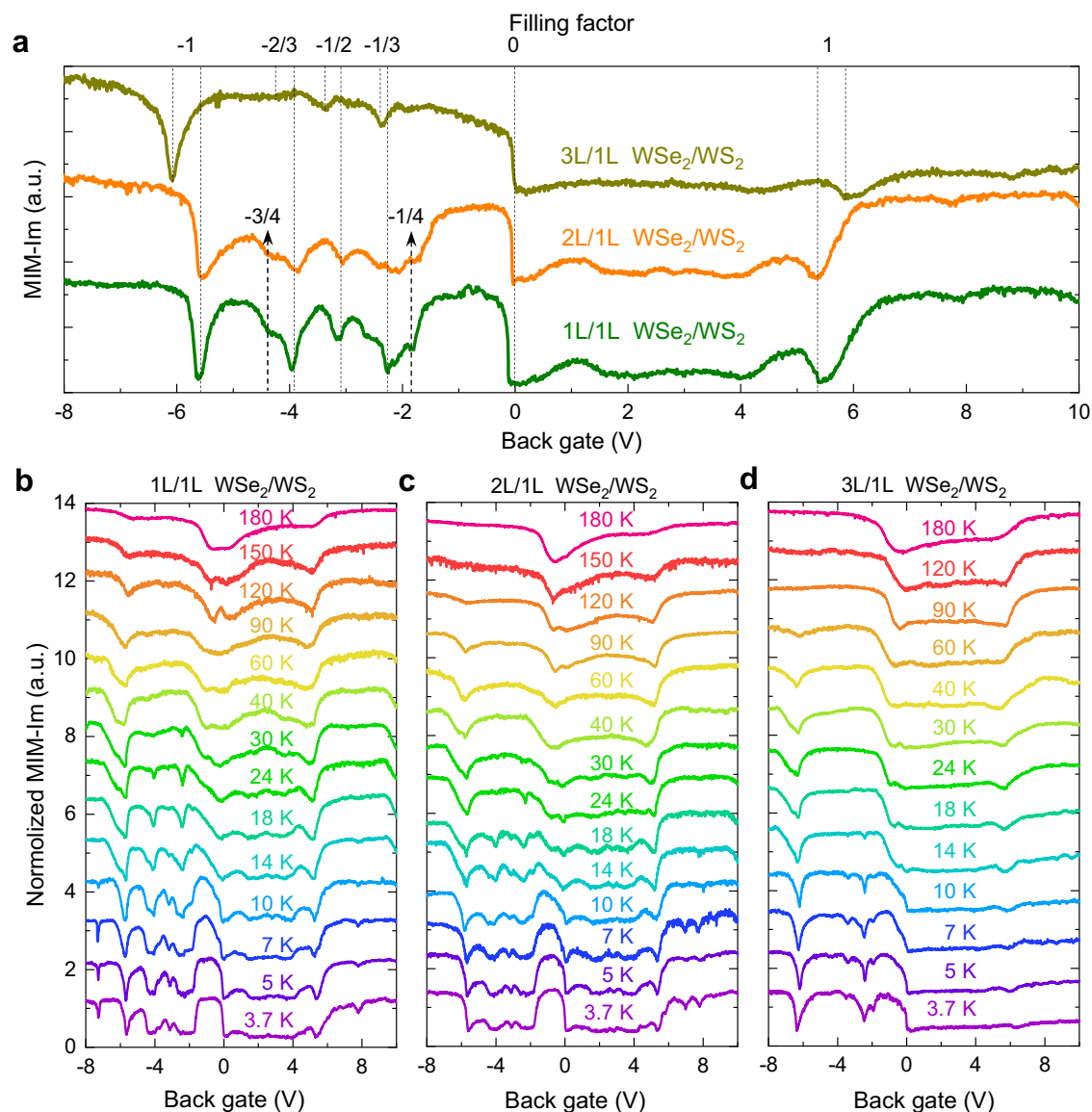


Fig. 4 | MIM measurements of correlated states in different moiré superlattices. **a** MIM spectra as a function of gate voltage for the moiré superlattice of 1L/1L WSe₂/WS₂ (green), 2L/1L WSe₂/WS₂ (orange), and 3L/1L WSe₂/WS₂ (brown) at

10 K. **b–d** are the temperature-dependent MIM spectra for the moiré superlattice of 1L/1L, 2L/1L, and 3L/1L WSe₂/WS₂, respectively.

MIM signals. In this paper, we simply refer to $d(\text{MIM})/dz$ as the MIM signal.

Estimating the twist angle

Twist angles of the moiré superlattices can be estimated by the carrier density corresponding to the correlated insulating state at $n = \pm 1$, with a bottom hBN of thickness ~ 52 nm and dielectric constant 3.5. The 1L/1L WSe₂/WS₂ and 2L/1L WSe₂/WS₂ regions have a similar moiré periodicity of 7.4 nm and twist angle of 0.9°. For the 3L/1L WSe₂/WS₂ region, the moiré periodicity is 6.0 nm and the twist angle is 1.3°. This difference is likely caused by a small distortion or wrinkle between WSe₂ and WS₂ layers.

Data availability

Source data are available for this paper. All other data that support the plots within this paper and other findings of this study are available from the corresponding author upon reasonable request.

Code availability

The source code for the numerical simulations is available from the corresponding author upon reasonable request.

References

1. Cao, Y. et al. Correlated insulator behaviour at half-filling in magic-angle graphene superlattices. *Nature* **556**, 80–84 (2018).
2. Cao, Y. et al. Unconventional superconductivity in magic-angle graphene superlattices. *Nature* **556**, 43–50 (2018).
3. Chen, G. et al. Evidence of a gate-tunable Mott insulator in a trilayer graphene moiré superlattice. *Nat. Phys.* **15**, 237–241 (2019).
4. Bistritzer, R. & MacDonald, A. H. Moiré bands in twisted double-layer graphene. *Proc. Natl Acad. Sci.* **108**, 12233–12237 (2011).
5. Sharpe, A. L. et al. Emergent ferromagnetism near three-quarters filling in twisted bilayer graphene. *Science* **365**, 605–608 (2019).
6. Serlin, M. et al. Intrinsic quantized anomalous Hall effect in a moiré heterostructure. *Science* **367**, 900–903 (2020).
7. Chen, G. et al. Tunable correlated Chern insulator and ferromagnetism in a moiré superlattice. *Nature* **579**, 56–61 (2020).

8. Shen, C. et al. Correlated states in twisted double bilayer graphene. *Nat. Phys.* **16**, 520–525 (2020).
9. Cao, Y. et al. Tunable correlated states and spin-polarized phases in twisted bilayer–bilayer graphene. *Nature* **583**, 215–220 (2020).
10. Liu, X. et al. Tunable spin-polarized correlated states in twisted double bilayer graphene. *Nature* **583**, 221–225 (2020).
11. Chen, S. et al. Electrically tunable correlated and topological states in twisted monolayer–bilayer graphene. *Nat. Phys.* **17**, 374–380 (2021).
12. Polshyn, H. et al. Electrical switching of magnetic order in an orbital Chern insulator. *Nature* **588**, 66–70 (2020).
13. Shi, Y. et al. Tunable van hove singularities and correlated states in twisted trilayer graphene. *Nat. Phys.* **17**, 619–626 (2021).
14. Chen, G. et al. Signatures of tunable superconductivity in a trilayer graphene moiré superlattice. *Nature* **572**, 215–219 (2019).
15. Regan, E. C. et al. Mott and generalized Wigner crystal states in WSe_2/WS_2 moiré superlattices. *Nature* **579**, 359–363 (2020).
16. Chu, Z. et al. Nanoscale conductivity imaging of correlated electronic states in WSe_2/WS_2 moiré superlattices. *Phys. Rev. Lett.* **125**, 186803 (2020).
17. Tang, Y. et al. Simulation of Hubbard model physics in WSe_2/WS_2 moiré superlattices. *Nature* **579**, 353–358 (2020).
18. Xu, Y. et al. Correlated insulating states at fractional fillings of moiré superlattices. *Nature* **587**, 214–218 (2020).
19. Huang, X. et al. Correlated insulating states at fractional fillings of the WS_2/WSe_2 moiré lattice. *Nat. Phys.* **17**, 715–719 (2021).
20. Miao, S. et al. Strong interaction between interlayer excitons and correlated electrons in WSe_2/WS_2 moiré superlattice. *Nat. Commun.* **12**, 3608 (2021).
21. Zhou, Y. et al. Bilayer Wigner crystals in a transition metal dichalcogenide heterostructure. *Nature* **595**, 48–52 (2021).
22. Smoleński, T. et al. Signatures of Wigner crystal of electrons in a monolayer semiconductor. *Nature* **595**, 53–57 (2021).
23. Wang, L. et al. Correlated electronic phases in twisted bilayer transition metal dichalcogenides. *Nat. Mater.* **19**, 861–866 (2020).
24. Qiu, D. Y., da Jornada, F. H. & Louie, S. G. Optical spectrum of MoS_2 : many-body effects and diversity of exciton states. *Phys. Rev. Lett.* **111**, 216805 (2013).
25. Ye, Z. et al. Probing excitonic dark states in single-layer tungsten disulphide. *Nature* **513**, 214–218 (2014).
26. Chernikov, A. et al. Exciton binding energy and nonhydrogenic Rydberg series in monolayer WS_2 . *Phys. Rev. Lett.* **113**, 076802 (2014).
27. Ugeda, M. M. et al. Giant bandgap renormalization and excitonic effects in a monolayer transition metal dichalcogenide semiconductor. *Nat. Mater.* **13**, 1091–1095 (2014).
28. Yu, H., Liu, G., bin, Tang, J., Xu, X. & Yao, W. Moiré excitons: from programmable quantum emitter arrays to spin-orbit–coupled artificial lattices. *Sci. Adv.* **3**, e1701696 (2017).
29. Wu, F., Lovorn, T. & Macdonald, A. H. Topological exciton bands in moiré heterojunctions. *Phys. Rev. Lett.* **118**, 147401 (2017).
30. Mak, K. F., Lee, C., Hone, J., Shan, J. & Heinz, T. F. Atomically thin MoS_2 : a new direct-gap semiconductor. *Phys. Rev. Lett.* **105**, 136805 (2010).
31. Splendiani, A. et al. Emerging photoluminescence in monolayer MoS_2 . *Nano Lett.* **10**, 1271–5 (2010).
32. Jin, C. et al. Observation of moiré excitons in WSe_2/WS_2 heterostructure superlattices. *Nature* **567**, 76–80 (2019).
33. Li, H. et al. Imaging moiré flat bands in three-dimensional reconstructed WSe_2/WS_2 superlattices. *Nat. Mater.* **20**, 945–950 (2021).
34. Shimazaki, Y. et al. Optical signatures of periodic charge distribution in a Mott-like correlated insulator state. *Phys. Rev. X* **11**, 021027 (2021).
35. Yu, H. et al. Dirac cones and Dirac saddle points of bright excitons in monolayer transition metal dichalcogenides. *Nat. Commun.* **5**, 3876 (2014).
36. Wu, F. et al. Exciton band structure of monolayer MoS_2 . *Phys. Rev. B* **91**, 075310 (2015).
37. Hsu, W. et al. Tailoring excitonic states of van der Waals bilayers through stacking configuration, band alignment, and valley spin. *Sci. Adv.* **5**, eaax7407 (2019).
38. Jones, A. M. et al. Spin–layer locking effects in optical orientation of exciton spin in bilayer WSe_2 . *Nat. Phys.* **10**, 130–134 (2014).
39. Wang, L. et al. One-dimensional electrical contact to a two-dimensional material. *Science* **342**, 614–617 (2013).

Acknowledgements

We thank professor Feng Wang and professor Chenhao Jin for their helpful discussions. The optical spectroscopy measurements are supported by an AFOSR DURIP award through Grant FA9550-20-1-0179. The device fabrication was supported by the Micro and Nanofabrication Clean Room (MNCR) at Rensselaer Polytechnic Institute (RPI). Z. Lian and S.-F.S. acknowledge support from NYSTAR through Focus Center-NY-RPI Contract C150117. S.-F.S. also acknowledges the support from NSF (Career Grant DMR-1945420 and DMR-2104902) and AFOSR (FA9550-18-1-0312). X.H. and Y.-T.C. acknowledge support from NSF under award DMR-2104805. Y.S. and C.Z. acknowledge support from NSF PHY-2110212, PHY-1806227, ARO (W911NF17-1-0128), and AFOSR (FA9550-20-1-0220). D.C. acknowledges support from the National Natural Science Foundation of China, Grant number 62004032. S.T. acknowledges support from NSF DMR-1904716, DMR-1838443, CMMI-1933214, and DOE-SC0020653. K.W. and T.T. acknowledge support from the Elemental Strategy Initiative conducted by the MEXT, Japan, Grant Number JPMXP0112101001 and JSPS KAKENHI, Grant Numbers 19H05790 and JP20H00354. L.X. and D.S. acknowledge support from the U.S. Department of Energy (no. DE-FG02-07ER46451) for magneto-spectroscopy measurements performed at the National High Magnetic Field Laboratory, which is supported by the National Science Foundation through NSF/DMR-1644779 and the State of Florida.

Author contributions

S.-F.S. and Y.-T.C. conceived the project. D.C. and Z.L. fabricated the heterostructure devices and performed the optical spectroscopy measurements. X.H. performed the MIM measurements. M.R. helped with device fabrication. M.B. and S.T. grew the TMDC crystals. T.T. and K.W. grew the BN crystals. C.Z. and Y.S. performed the theoretical calculations. S.-F.S., Y.-T.C., C.Z., Y.S., D.C., Z.L., Z.W., X.H., and L.Y. analyzed the data. S.-F.S. and Y.-T.C. wrote the manuscript with inputs from all authors.

Competing interests

The authors declare no competing interests.

Additional information

Supplementary information The online version contains supplementary material available at <https://doi.org/10.1038/s41467-022-32493-9>.

Correspondence and requests for materials should be addressed to Zenghui Wang, Chuanwei Zhang, Yong-Tao Cui or Su-Fei Shi.

Peer review information *Nature Communications* thanks the anonymous reviewers for their contribution to the peer review of this work. Peer reviewer reports are available.

Reprints and permission information is available at <http://www.nature.com/reprints>

Publisher's note Springer Nature remains neutral with regard to jurisdictional claims in published maps and institutional affiliations.

Open Access This article is licensed under a Creative Commons Attribution 4.0 International License, which permits use, sharing, adaptation, distribution and reproduction in any medium or format, as long as you give appropriate credit to the original author(s) and the source, provide a link to the Creative Commons license, and indicate if changes were made. The images or other third party material in this article are included in the article's Creative Commons license, unless indicated otherwise in a credit line to the material. If material is not included in the article's Creative Commons license and your intended use is not permitted by statutory regulation or exceeds the permitted use, you will need to obtain permission directly from the copyright holder. To view a copy of this license, visit <http://creativecommons.org/licenses/by/4.0/>.

© The Author(s) 2022